ELSEVIER

Contents lists available at ScienceDirect

Surface Science

journal homepage: www.elsevier.com/locate/susc



Influence of surface etching and oxidation on the morphological growth of Al_2O_3 by ALD



Mikhail Trought^a, Isobel Wentworth^b, Chathura de Alwis^a, Timothy R. Leftwich^c, Kathryn A. Perrine^a,*

- ^a Department of Chemistry, Michigan Technological University, Houghton, MI 49931, United States
- ^b Department of Chemical Engineering, Michigan Technological University, Houghton, MI 49931, United States
- ^c Department of Materials Science and Engineering, Michigan Technological University, Houghton, MI 49931, United States

ARTICLE INFO

Keywords: Surface functionalization Graphite oxidation Morphology Selective deposition ALD

ABSTRACT

Selective deposition using atomic layer deposition has potential as a viable method for growing patterned nanostructured materials, thus advancing the design of next-generation electronics and catalysts. This study investigated how etching HOPG produces different densities of functional groups and different morphologies that were found to influence the growth of Al_2O_3 structures. Hydrochloric acid produced a high density of -OH and -COOH functional sites on terrace regions on HOPG in comparison to nitric acid that produced -OH functional sites at defects. After exposure to ALD cycles of trimethylaluminum and water, different structures of Al_2O_3 were found to grow on the functional sites compared to defect sites. Field emission scanning electron microscopy, atomic force microscopy and Raman spectral imaging were used to characterize the changes in surface topography after etching and ALD. Vibrational spectroscopy and X-ray photoelectron spectroscopy were used to measure surface functionalization and quantify Al_2O_3 growth. Results suggest that the Al_2O_3 nucleation and growth at submonolayer coverage is affected by the surface functionalization as well as the topography and density of functional sites. This study finds that selective deposition on active areas are determined by the morphology and the functional groups that depend on the etching mechanism with the surface. These results suggest that understanding both the topography and type of functional site are necessary for designing the next-generation electronic devices and catalysts.

1. Introduction

Area-selective atomic layer deposition (ALD) has potential as a viable method for growing monolayer metal and metal oxide films for the next-generation of electronic devices, heterogeneous catalysts and other nanomaterials [1–7]. Deposition methods for fabrication of nanopatterned devices rely on top-down lithography methods to protect select areas on a surface prior to (metal or metal oxide) deposition [4,5,8–10]. However, these methods use photochemical masks, etching and other chemical treatments that are specific to the substrate and lead to possible contamination, edge placement problems, and expensive chemical consumption [10]. If bottom-up approaches could be utilized, the need for these expensive lithography steps could be minimized or even eliminated.

Area-selective ALD by area-activation is one route towards selective

deposition that does not require multiple lithography steps [4]. The idea is that reactive sites, such as surface functional groups, are strategically seeded on a specific area of the surface, leaving the remaining surface with a lower possibility of reaction [11–13]. The surface is then exposed to ALD precursors that react only with the activated area, resulting in film or nanoparticle growth. This method could yield new avenues for tailored metal and metal oxide deposition with better control on the atomic scale. Recent studies [5,14–16] have shown that deposition of particles at submonolayer coverages can be used for preliminary steps in etching mechanisms and for heterogeneous catalyst design [1–3,17]. These methods are currently in the early stages of development for selective area deposition [4,11,18]. Using ALD to deposit materials at specific surface sites will rely on surface limited reactions that are initiated by surface functional groups for atomic layer growth [19,20] and the morphology of functional sites. However,

Abbreviations: ALD, atomic layer deposition; TMA, trimethylaluminum; XPS, X-ray photoelectron spectroscopy; AFM, atomic force microscopy; FESEM, field emission scanning electron microscopy; ATR-FTIR, attenuated total reflectance-Fourier transform infrared spectroscopy

E-mail address: kaperrin@mtu.edu (K.A. Perrine).

^{*} Corresponding author.

understanding the surface chemistry and topography is necessary to have control over the reaction between the active sites and the metalorganic precursors required for selective deposition.

Graphene technology impacts industries, from nanoelectronics to batteries and catalysts due to its unique electronic properties, thermal stability and mechanical strength from the sp2 hybridized aromatic hydrocarbon sheets [5,21-32]. The surface of graphene has been modified by oxidation to form graphene oxide, which can be used to tune the properties for various new applications [30,33-35]. This structure enables the possibility for growing metal nanostructures on the surface. It is well known that trimethylaluminum (TMA) and water. is the ideal reaction for ALD, where TMA reacts selectively with -OH functional groups [13,36]. Several groups [30,37–39] have investigated the formation of graphene oxide and carbon nanotubes, which produce a multitude of oxygenated functional groups. Others have investigated ALD reactions on highly oriented pyrolytic graphite (HOPG), a model surface for graphene [28,34,40], and observed that Al₂O₃ deposits on defects and step edges, owing to the reaction of the CH3 ligands with the sp³ carbon edges, thus enabling nucleation at the defect areas in comparison to the terrace regions. Other ALD precursors, such as Pt, have also been examined on bare HOPG to find that Pt selectively grows on defects, depending if water or ozone is used as a co-reactant [5,41-43].

For area activation ALD, it is beneficial to start with an unreactive surface that could then become activated with reactive "seed" sites or functional groups [1,11,30,39]. 2D materials are advantageous for selective functionalization that may not require lithography steps due to the stability of their layers of sheets. This study used HOPG as a model 2D material, graphene, where the terraces of the carbon sheets are chemically unreactive in ambient conditions, while their defects are highly reactive [44–49]. These defects, typically found at the step edges, have been shown to act as nucleation sites for metal deposition [41,44,47,49–52].

In this study we show how the etching of HOPG with different acids prior to ALD produces different growth of Al_2O_3 on HOPG. The influence of graphite functionalization and surface topography changes, from oxidative etching, on ALD growth on HOPG were investigated. This is attributed to the etching mechanism of HOPG with the different acids: HCl was found to etch the terrace regions and HNO $_3$ was found to etch the defect regions. The ALD reaction of TMA and water is used to grow Al_2O_3 on the defect sites and the oxygen functional sites. At submonolayer coverage, different growth morphologies are observed, when different acids are used prior to ALD, which could be used for further deposition as heterogeneous catalysts systems or in electronic devices.

2. Materials and methods

2.1. Surface preparation

Highly oriented pyrolytic graphite samples (10 mm × 10 mm, ZYB quality, MikroMasch USA.) were prepared by cross sectioning the HOPG into 5 mm × 10 mm samples. The adhesive tape method [53] was used to cleave a fresh surface yielding a mirror-like finish. Tailored defects were created by bombarding the cleaved HOPG using a focused ion beam (FIB, Hitachi) instrument using a gallium source at 30 keV source with a beam deceleration voltage of $8.8\,kV$ and $3.2\,\mu A$, a beam diameter of 20 nm and a 100 µs dwell time. No gallium was detected on the samples, according to XPS analysis. Arrays of tailored defects of uniform shapes (1 µm² squares or 0.43 µm² triangular areas) were created in $20\,\mu m \times 20\,\mu m$ areas on the HOPG surface. This allowed for consistent fabrication of controllable step edges (~ 1 nm in depth) and defect areas to test for metal oxide growth before and after surface functionalization and ALD. Patterned HOPG samples were then functionalized with oxygenated functional groups by etching with two different acids. A droplet of either pure 15.8 M nitric acid (HNO₃, 70%,

Sigma Aldrich) or 12.1 M hydrochloric acid (HCl, 36%, Sigma Aldrich) was carefully placed (using a clean glass pipette) onto the patterned HOPG sample for 2 h at room temperature. This was done to only allow the acid to react with the top surface layers and to prevent penetration through the sides of the HOPG and reduce intercalation of the acid though the graphene sheets [54–56]. After etching, the samples were rinsed with 50 mL of ultra-pure water (Milli-Q water 18M Ω -cm) and allowed to air dry.

2.2. Atomic layer deposition (ALD)

Acid-treated (oxidized) and untreated HOPG samples were placed in a thermal ALD (Savannah, Cambridge Nanotech) system at the University of Minnesota Nanocenter and exposed to cycles (1 Å/cycle) of TMA and $\rm H_2O$ at 150 °C. The untreated HOPG, HNO3 etched HOPG and HCl etched HOPG were separately exposed to 2, 5, 10 and 25 cycles of ALD. The $\rm Al_2O_3$ growth was calibrated by ALD deposition on SiO2 wafers. SiO2 wafers (5 mm \times 10 mm) were also placed in the ALD system during each deposition for each sample to check for uniform deposition rate. The amount of $\rm Al_2O_3$ grown on the SiO2 was verified by ellipsometry (Gaertner LSE Stokes Ellipsometer).

2.3. Surface analysis

The samples were characterized before and after oxidation as well as after ALD using several spectroscopy and microscopy techniques. X-ray photoelectron Spectroscopy (XPS) and attenuated total reflection Fourier transform infrared spectroscopy (ATR-FTIR) were used to verify surface functionalization, and to quantify ALD and elemental composition. Field emission scanning electron microscopy (FESEM), atomic force microscopy (AFM) and confocal Raman microscopy were used to observe the morphological changes, measure surface roughness and confirm particle or film growth on the treated HOPG surfaces after deposition of Al_2O_3 .

The XPS spectra were recorded with a PHI 5800 photoelectron spectrometer using a Mg X-ray source operated at 400 W. Spectra were collected in an area with a nominal diameter of 800 µm. Survey spectra were collected using a pass energy of 187.85 eV, a dwell time of 20 ms/ step and a resolution of 0.8 eV/step. High resolution spectra were collected using a pass energy of 23.50 eV, a dwell time of 100 ms/step and a resolution of 0.1 eV/step. All XPS data were charge corrected using the sp² C1s peak at 284.6 eV for graphite as the reference [37]. High resolution XPS regions of O1s, N1s, Cl2p, C1s, Al2p were fitted as follows. All regions except the C1s region were fitted using a Shirley background [57] and 100% Gaussian peak deconvolution. The C1s region was fit using a Tougaard background [58–60] and the sp² carbon peak (at 284.6 eV) was fit using the asymmetric Doniach-Šunjić lineshape [61,62]. The remaining peaks under the C1s region were fit using 100% Gaussian peaks. This resulted in a better overall fit and accounted for more of the tailing region of the sp² graphitic carbon peak. The N1s and Cl2p were scanned to check for residual surface species from the HCl and HNO3 etching. No evidence of either of these elements was observed, thus resulting in production of oxygenated functional groups on the HOPG surface, in agreement with previous findings [55,63].

ATR-FTIR spectra were recorded on a Nicolet iS50R (ThermoFisher Scientific Inc.) in the PI's lab at Michigan Technological University on a diamond ATR cell, using 256 scans and a resolution of 4 cm⁻¹. The HOPG surface was referenced to the diamond ATR cell as a background spectrum. Unetched HOPG samples after ALD samples were referenced to a blank HOPG sample, and acid-etched samples exposed to ALD were referenced to the respective acid-etched HOPG sample.

FESEM images were collected using a Hitachi S-4700 microscope using an accelerating voltage of 10 kV, a beam current of 10 $\mu A,$ a working distance of 7 mm, and a 40 ms dwell time. Prior to FESEM, the HOPG samples were mounted on an aluminum SEM sample holder that contained copper clips to pin down the sample, which also helped to

reduce charging across the HOPG surface.

AFM images were collected on an Asylum MFP-3D Origin microscope with areas of 5 $\mu m^2,~3.2~\mu m^2,~and~1.4~\mu m^2$ using 256 points per line. Images were collected using an aluminum-coated silicon tip (Budget Sensors) with a frequency of 300 kHz in tapping mode and a force constant of 40 N/m. Images were post processed using a 3rd order flattening and masking. Root mean squared (RMS) values were analyzed for surface roughness by analyzing several areas of the terrace region of each sample before and after ALD. Values are reported as an average with a standard deviation of the mean.

Confocal Raman microscopy images were collected on a Witec alpha 300 R at the University of Minnesota's Nanocenter. Images were collected using an excitation wavelength of 532 nm and 600 grooves/mm grating using an integration time of 0.15 s, scan speed of 7.5 s/line, 50 points per line over a $6\times6~\mu\text{m}^2$ area. A depth scan (1–4 $\mu\text{m})$ was collected to obtain the surface region before collecting the microscopy Raman images. The Raman image was then collected at the surface region averaging over 6.25 min for high-resolution imaging of each triangular defect area.

3. Results and discussion

3.1. Surface Functionalization of HOPG

The HOPG surface was functionalized by acid etching with two different acids, HCl and HNO3, separately. Surface functionalization of the HOPG samples was characterized using ATR-FTIR, XPS and FESEM. The ATR-FTIR spectroscopy was used to qualitatively identify and analyze the vibrational signatures of surface functional groups before and after oxidation with concentrated HNO3 and HCl. The infrared vibrational spectra are complemented with XPS to identify and quantify the surface functional groups before and after ALD in Fig. 1A and B. Representative data of the samples are shown before and after acid etching. In the HOPG spectrum, there is a negative absorption peak from the in-plane C=C stretching (E_{1u} band) at 1585 cm⁻¹ [64]. The strong, sharp negative absorbance is attributed to a difference in refractive index and reflectivity of HOPG, as was also observed for diamond [65]. The C-C stretching (A_{2u} band) mode is due to the stretching between the graphene sheets, and is observed as an intense, sharp positive absorption peak at 870 cm⁻¹. The strong negative peak at $1075~\text{cm}^{-1}$ is due to an artifact of the diamond ATR cell or DLaTGS detector, as it is present in other samples. No strong stretching from surface hydroxyl groups is apparent on the bare HOPG surface, as

expected. After acid etching the HOPG samples with either HNO3 or HCl, using the bare HOPG surface's infrared spectrum as a background, stretching from hydroxyl functional groups appear between 3300-3700 cm⁻¹. These results are in agreement with previously observed results, suggesting that both acid-etched surfaces contain hydroxyl functional groups [30,54,55,66]. Although some of the O-H stretch region could be due to physisorbed water, the XPS spectra unambiguously measures the presence of oxygenated surface species on the acid treated surface, as discussed below. The difference between how the HNO3 and HCl acids etch the HOPG surface becomes apparent in the fingerprint region. For the HCl etched HOPG samples, there is a strong C=O stretch at 1730 cm⁻¹ that suggests the presence of the -COOH functional group on the surface [30,37,55,66,67]. Only OH-stretching is observed in the ATR-FTIR spectrum of HNO3-etched HOPG and no additional vibrational frequencies are observed suggesting that this surface is functionalized with -OH groups. It should be noted that the presence of N-O, NO₂ or C=O groups were not observed when the sample is etched with HNO₃ as was observed for gas phase functionalization with HNO₃ [68]. These vibrational identities are corroborated with XPS results.

The O1s region was used to track the oxidation of the HOPG surfaces after acid etching. The spectra in this region were deconvoluted using 100% Gaussian distributions. The O1s region in Fig. 1C shows that before acid etching, no observable oxygen is present on the HOPG surface. After etching with either $\rm HNO_3$ or HCl, an oxygen peak appears at 533.4 eV on both samples, which can be assigned to the hydroxyl functional group (-OH), as observed from previous studies [55,63,66]. An additional minor peak at 535.3 eV is present on the HCl etched HOPG samples, in agreement with the ATR-FTIR spectrum that a carboxylic acid group (-COOH) is also present on the surface [21].

The C1s region in Fig. 1D was deconvoluted using the Doniach-Šunjić asymmetric fit [58,61,62] for the first peak, which is the sp² C1s peak at 284.6 eV, and 100% Gaussian distributions for the remaining peaks. We rationalize these fits based on the success of applying these fits to other graphitic materials in the C1s region [58,69]. The second peak at 285.3 eV is present on all three types of surfaces and likely can be assigned to sp³ carbon [70]. The C1s peak at 286.0 eV is assigned to the C–OH functional group on both the HNO₃-etched and HCl-etched HOPG samples, as observed and confirmed by previous derivatization reactions [55,63,66]. There is a small peak at 288.0 eV from the contribution of the -COOH functional group on the HCl-etched HOPG, in agreement with the ATR-FTIR and O1s results. Although the Doniach-Šunjić asymmetric fit was a good fit for the sp² carbon, it did not account for the area under the remaining part of the curve on unetched

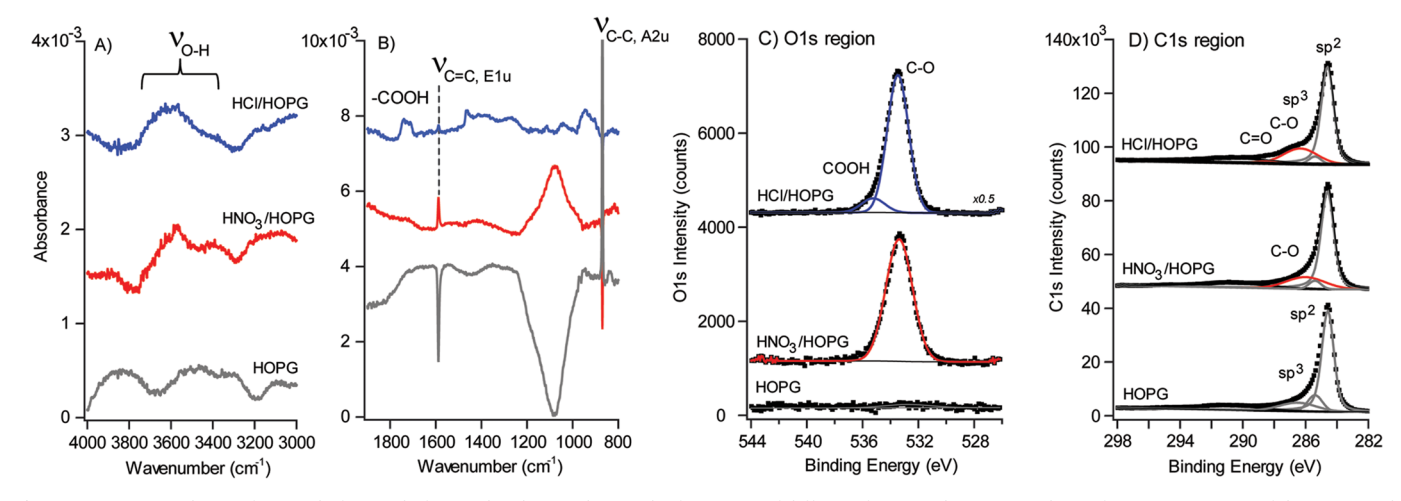


Fig. 1. ATR-FTIR and XPS of HOPG before and after acid etching indicates the formation of different functional groups on the surface. A) ATR-FTIR of the OH stretch region, B) ATR-FTIR of the fingerprint region, C) O1s XPS region and D) C1s XPS comparing the three different HOPG surfaces. HNO₃ etched HOPG results in OH-functionalized HOPG and HCl etched HOPG results in a combination of –OH and -COOH functional groups. O1s and C1s XPS spectra shows the HOPG samples before and after acid etching showing the formation of different functional sites.

HOPG. The remaining portion of the signal in the C1s region was fit using Gaussian lineshapes at similar positions to the acid-etched HOPG samples for comparison before and after oxidation. The shape of the C1s region for the unetched HOPG is consistent with what has been observed elsewhere for graphite [69-71]. An average area of the C-O peak in the XPS spectrum of the HOPG surface was observed as 10.3% of the C1s region. A small amount of 0.6% oxygen was present on the HOPG surface in the O1s region likely from exposure to ambient conditions. After acid etching, the C-O area increased to 17.9% of the C1s region for HNO3-etched HOPG and 14.6% of the C1s region for HCletched HOPG, with 3.8% for the -COOH functional group. Only subtle changes in the FWHM of the C-O peak in the C1s region on the oxidized HOPG surfaces were observed: a small increase for the HNO3etched HOPG and a clear shoulder observed for the HCl-etched HOPG, in Fig. 1D. The O1s region unambiguously indicates the surface oxidation of the top few layers of the acid-etched HOPG surfaces, as shown in Fig. 1C. Together, both ATR-FTIR and XPS data show that the HOPG surface was oxidized by acid etching and results in different functional groups, producing an -OH functionalized surface for the HNO3-etched HOPG and a mixture of -OH and -COOH functional groups for the HCletched HOPG.

Interesting changes in surface morphology are produced from etching the HOPG surface with different acids. FESEM images are shown in Fig. 2 illustrate the differences between etching with HNO₃ (B) and HCl (C) after 6 h in comparison to a freshly cleaved HOPG surface (A). AFM images are shown below each respective FESEM image to compare the differences in surface topography after 2 h of etching. As seen in the HNO3-etched HOPG (Fig. 2B) when compared with the visible step edges on plain HOPG (Fig. 2A), the HNO₃ appears to etch the step-edge defects in addition to providing smaller point defects on the terraces. In contrast, the HCl appears to etch through the top sheets of the HOPG terraces (Fig. 2C), resulting in holes and a weblike morphology, possibly etching through the top layers of graphene sheets. Surface roughness values were recorded as RMS values. The surface roughness (measured on the terrace region) was an average of 0.24 nm for HNO3-etched HOPG and 0.28 nm for HCl-etched HOPG, as compared to untreated HOPG of 0.07 nm. This difference in topography, despite the fact that both acids produce -OH functional groups on HOPG, yield different metal oxide nucleation at these site as described below. Our group is further investigating the effect that acids have on the HOPG surface in order to connect surface sites with topographical changes (to be published).

3.2. ALD of Al₂O₃ on functionalized HOPG

After etching, the effect of submonolayer growth of ALD Al₂O₃ on HOPG was observed using FESEM. Fig. 3 shows the FESEM images of HOPG with square defects of 1 µm2 in area before and after HNO3 and HCl etching that result in different topographical changes to the HOPG surface. It should be noted that the square defects fabricated by the FIB instrument were used to create uniform sized defects to track the changes at these sites and to probe the growth of Al₂O₃, thus comparing between the defected area and terrace regions. The terrace regions also have natural step edges, which also participate in the reaction with TMA upon ALD. After the HOPG was FIB patterned with tailored defects and etched with acid, the samples were placed in a thermal ALD system and exposed to TMA and H₂O cycles at 150 °C. ALD on the untreated, HNO₃-etched and HCl-etched HOPG reveal the growth of Al₂O₃ on the samples is drastically different at submonolayer coverage (Fig. 3). FESEM was used to image the samples after ALD and AFM was used to quantify the particle dimensions (height and length) and film roughness (root mean squared - RMS value) on the functionalized HOPG surfaces. The AFM images after ALD exposure to the HNO3-etched, HCl-etched and unetched HOPG is shown in Figure S1 in the supporting information section.

With the deposition of 2 ALD cycles on untreated HOPG, the ${\rm Al_2O_3}$ deposits primarily on the square defect regions with minor deposition on the terraces, as shown in Fig. 3. This is due to the reaction of the trimethyl ligands with the sp³ carbon, as has been observed previously [28]. Upon increasing ALD cycles from 5 to 25 cycles, the ${\rm Al_2O_3}$ grows inside the square defected area and at the defect edges with minimal ${\rm Al_2O_3}$ on the terrace region.

ALD of submonolayer coverage on the HNO $_3$ -etched HOPG results in particle growth of ${\rm Al}_2{\rm O}_3$ on the step edges of both the square defects and terrace regions. This may be due to the etching producing high density –OH functional groups on the defect sites and pinholes on the terrace region. We provide more evidence and discuss this throughout the text. After 2 ALD cycles, the particles grow to roughly an average of 124 nm in diameter and 6.2 nm in height in the defect region and the particles on the terrace region are 45 nm in diameter and 5.8 nm in

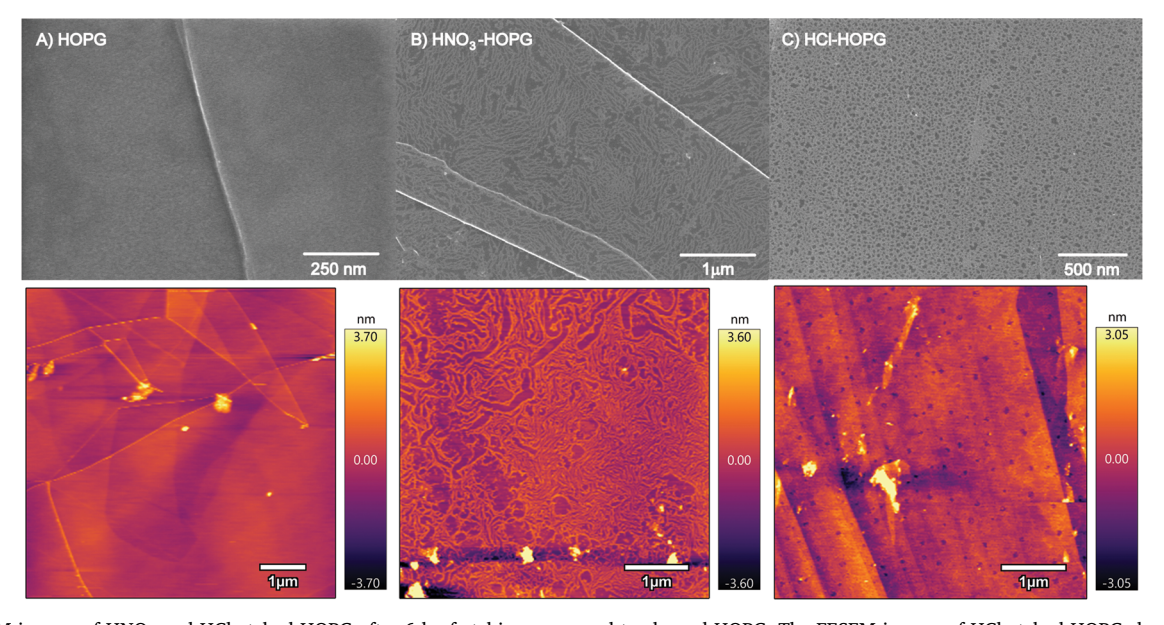


Fig. 2. FESEM images of HNO_3 and HCl-etched HOPG after 6 h of etching compared to cleaved HOPG. The FESEM images of HCl-etched HOPG shows a web-like topography post etching, whereas the HNO_3 -etched HOPG produces step edges and defect pinholes on the HOPG defect. AFM images confirm the surface topography post etching after 2 h.

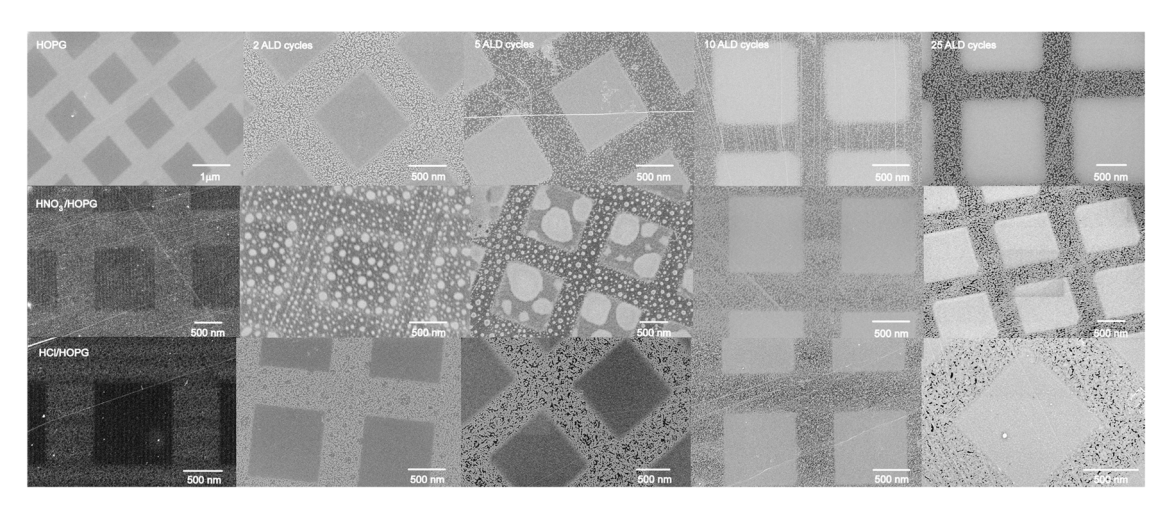


Fig. 3. FESEM of FIB patterned HOPG and acid etched HOPG exposed to ALD cycles of TMA and water at 150 °C. The five columns of FESEM images represent the number of ALD cycles for each surface and are, from left to right: 0 ALD cycles, 2 ALD cycles, 5 ALD cycles, 10 ALD cycles and 25 ALD cycles. The three rows of FESEM images represent how the surface was treated prior to ALD cycles and are, from top to bottom: untreated HOPG, HNO₃-etched HOPG and HCl-etched HOPG. Al₂O₃ nucleates and grows at defect areas at submonolayer coverage on untreated HOPG and HNO₃-etched HOPG. On HCl-etched HOPG, Al₂O₃ nucleates on the functional sites on the terrace regions of oxidized HOPG resulting in film growth.

height, as analyzed by AFM (see Figure S1 in the supporting information). When the HNO3-etched samples are compared to the unetched HOPG samples, this suggests that the functionalized -OH sites affect the nucleation and growth of ALD Al₂O₃. After increasing the number of ALD cycles to 5 (separate deposition on a newly prepared sample), the particles selectively grow into larger Al₂O₃ platelets inside the square defect areas, with an average of 333 nm in diameter and 8.1 nm in height. The particles on the terrace region, in between the defect areas, grow into slightly larger particles with an average of 76 nm in diameter and 8.2 nm in height, but generally remain the same size compared to the sample with 2 cycle Al₂O₃ deposition. The particles appear to grow laterally (thus filling in with a film around the particles, which offsets the height measurement). As higher exposures are applied, (5 cycles) the particles grow laterally, not increasing significantly in height. After increasing to 10 ALD cycles, the particles appear to have grown into a partial film on the terrace regions and filled in the defect areas. After 25 ALD cycles, the Al₂O₃ fills the square defect region, producing threedimensional structures in the defect region on the HNO3-etched HOPG surface. The measured AFM line profile across the step edge of the square defects shows an increase of 3.1 nm in height from the terrace, demonstrating that the Al₂O₃ is selectively grown in the defect areas on the HNO₃-etched HOPG. The FESEM image after 25 ALD cycles on the HNO3-etched HOPG was taken using the secondary electron detector at a tilt angle of 45° to better image the 3D structure. Additional measurements were recorded using AFM (discussed below) to quantify the

On the HCl-etched HOPG surface, TMA reacts with the -OH and -COOH functional groups on the terrace sites at low exposures of 2 and 5 ALD cycles leaving the square defect areas unfilled. After 10 and 25 cycles, $\rm Al_2O_3$ grows in the defect area, thus producing a thin film across the terrace and defect area. This resulted in a height increase of only 0.38 nm from the terrace to the square defect for the 25 cycle sample. This suggests that the HCl reacts with mainly the basal plane of HOPG terrace producing a high density of reactive functional sites of primarily –OH and a minor concentration of –COOH groups across the surface, where the TMA reacts selectively on those sites to deposit $\rm Al_2O_3$ rather than at the defect sites in the square areas. After the functional groups on the terrace are consumed, it appears that the additional TMA then reacts with the $\rm Al_2O_3$ seed sites to fill in the defect areas at 25 ALD cycles, resulting in a thin film.

By comparing the topography and identities of the functional groups from the acid etching on the HOPG surface, it is apparent that the ${\rm Al_2O_3}$ grows at the oxygenated functional groups sites on both acid-etched

surfaces as opposed to the (sp³) defect sites, which are only present on the untreated HOPG surface. The differences are how the HNO3 and HCl-etched the surface leaving different densities of -OH functional groups on different regions of the HOPG surface. On the HNO3-etched HOPG, -OH groups were produced at the square defect sites and on small pinholes in the terrace, resulting in initial nucleation of Al₂O₃ at these sites (middle row, Fig. 3). As the ALD cycles increase from 2 to 5, the particles continue to grow at the defect areas, leaving the same smaller particles tethered at the pinholes on the terrace sites. For the HCl-etched HOPG, the Al₂O₃ nucleation occurs also on the -OH and -COOH groups on the HOPG terrace (bottom row, Fig. 3), and ultimately forms a thin film at high ALD exposures. This suggests the surface oxidation by acid etching with either HNO3 or HCl produces different topography and a different density of oxygen functional sites: where the HCl produces a large number of functional groups of primarily -OH and -COOH on the terraces and the HNO3 produces -OH functional groups on the defects. These sites alter the nucleation of Al₂O₃ during ALD, which may explain the differences in Al₂O₃ growth, producing either a film or particles, on the different areas on each surface.

To address whether the ALD resulted in the three dimensional growth on the different HOPG surfaces, AFM images (shown in Fig. S1, supporting information) were collected of the HOPG samples of submonolayer ALD coverage to quantify the surface roughness and additional features of the surface topography. Surface roughness values (shown in Fig. 4) were recorded as RMS values of the terrace height of all samples at submonolayer coverage. After ALD onto the different surfaces, the RMS values increased from their original values (discussed above), with the largest increase for HNO3-etched HOPG. These results are expected for materials that exhibit three-dimensional Volmer-Weber growth [72]. Particles are shown to nucleate and agglomerate on the defect regions of HNO₃-treated HOPG. The length and heights of the particles are reported above. Particles on the terrace region grow larger with additional ALD cycles, but remain small compared to the growth of Al₂O₃ platelets in the defect regions. The untreated HOPG and HCltreated HOPG samples have lower RMS values, but plateau around 1.0 nm. RMS values (not shown) were collected for 10 and 25 cycles and were found to plateau around 1.0 nm, as expected for film growth.

To compare the 3D growth on the three HOPG surfaces, the height was measured using a line profile across the step edge of the square defect area and the terrace of the HOPG surfaces, after 25 ALD cycles. The untreated HOPG, HCl-etched HOPG and HNO₃-etched HOPG samples resulted in height differences of 0.59 nm, 0.38 nm and 3.1 nm,

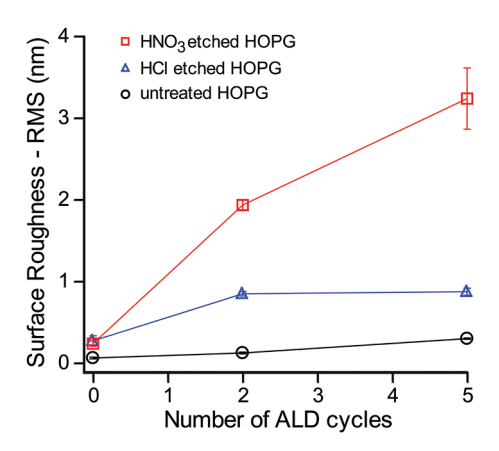


Fig. 4. Surface roughness plots from AFM images of ALD deposited ${\rm Al_2O_3}$ on functionalized HOPG surfaces at submonolayer coverage. These measurements indicate that the particle growth on the HNO3-etched HOPG resulted in the greatest roughness on the terrace region, with film growth on the HCl-etched HOPG and untreated HOPG.

respectively. Although all of the HOPG surfaces were exposed to 25 ALD cycles, there is a significant height increase in Al₂O₃ growth on the square defect areas for HNO3-etched HOPG. On the untreated HOPG and the HCl-etched HOPG, the deposited Al₂O₃ resulted in film growth across the defect areas and the terrace, as shown from the small difference in height. This suggests that the HNO₃ functionalizes the HOPG surface resulting in unique topography that yields selective growth of particles on the defect areas at submonolayer coverage. The HCl functionalizes the HOPG terrace region that also results in selective growth at low ALD exposures, but leaves the square defect region unreacted. After 25 ALD cycles, Al₂O₃ fills in the defect area, thus resulting in the small height difference of 0.38 nm. Compared to the untreated HOPG, where the Al₂O₃ reacts with the defect area (Fig. 3) at low coverage and after 25 ALD cycles, the Al₂O₃ fills in from the defect area across the terrace region. This data suggests that not only does density and type of functional group (-OH, -COOH, sp3) play a role in the reactivity with TMA during the ALD surface reaction, but also the placement of the functional groups. The mechanism in which HOPG is oxidized by either HNO₃ or HCl yields large scale topographical changes, which then seems to determine where the TMA will react, from the selective deposition on the functional group sites.

The differences of the growth by spectral identification and quantification methods were investigated using XPS and are discussed next. XPS of the HOPG samples were collected after ALD for the O1s, C1s and Al2p regions to quantify the deposition and growth of surface species. Example spectra from submonolayer (5 cycles) ALD exposures are shown in Fig. 5 (example spectra for each exposure shown in the supporting information in Figure S2). After 5 ALD cycles, the O1s peak areas increase on all HOPG samples, indicating that Al₂O₃ is deposited on HOPG, HNO3-etched HOPG, and HCl-etched HOPG. The O1s peak is centered at 533 eV with observed broadening, which increases with additional ALD cycles (shown as Figure S2). The Al-O species is observed at 531 eV, Al-OH, and any other carbon species would be observed at 533 eV [73–75]. Due to the overlapping of these peaks and the symmetric shape of the O1s region, it is difficult to deconvolute for these two species. The FWHM of the O1s region is roughly 2.26-2.56 eV on the etched HOPG samples and after deposition of 5 ALD cycles, the peak broadens to 2.8-2.9 eV, from the formation of amorphous Al₂O₃. This substantial broadening suggests there is an increase in Al-O deposition as well as some contribution from C-O species from unreacted -CH₃ ligands that are integrated into the Al₂O₃ material. This is further supported in the C1s region where the C-O species, centered at 286 eV (red peak in Fig. 5), increases with ALD cycles. In the Al2p region, only a single peak is observed at 75.5 eV, as expected for ALDwith TMA and

 $\rm H_2O$ at submonolayer coverage [28,76,77]. The majority of the surface species at 10 and 25 ALD cycles is present from the $\rm Al_2O_3$ peak at 75.5 eV, with a FWHM around 2.1 eV. At high ALD exposures at 10 and 25 cycles, a new minor species is formed at 77.3 eV that could be attributed to Al-OH.

In order to quantify the growth of the Al₂O₃ on the functionalized HOPG surfaces, the peak areas ratios were analyzed and compared. The peak area of the O1s, Al2p and the C-O peak in the C1s region were normalized to the sp² and sp³ C1s (substrate) area and plotted as a function of ALD cycle, as shown in Fig. 6. This was to account for the changes in sample height during the XPS analysis, as some of the HOPG samples were different thicknesses after cleaving them. We also refer the reader to example XPS spectra in Figure S2 to compare the different ALD exposures and Figure S3, example FESEM images of the terrace region after 5 ALD cycles. Fig. 6 shows that the Al2p/C1s(sp² and sp³) and O1s/C1s(sp² and sp³) ratios monotonically increase with increased ALD cycle, within experimental error. Each sample was exposed a single time to a specified number of ALD cycles prior to analysis and were not exposed to additional ALD cycles. For all surfaces the concentration of C-O (C1s(C-O)/C1s(sp² and sp³)) is increased, as shown in the C1s region, with increasing ALD cycles, suggesting that side reactions with the -CH₃ groups are grown into the Al₂O₃ material.

We notice there are two regions of interest: the submonolayer growth and the monolayer (film) growth. Below 10 ALD cycles, in the submonolayer growth regime, the Al₂O₃ particle nucleation is dominant and determined by the type of surface functional group, density of functional groups and surface topography. In Fig. 6, there is a statistically larger O1s/C1s(sp² and sp³), Al2p/C1s(sp² and sp³) and C1s (C-O)/C1s(sp² and sp³) ratios for the 5 ALD cycles on HCl-treated HOPG surface. This suggests the HCl-etched HOPG surface is highly reactive, allowing for more Al₂O₃ growth in the submonolayer region, in agreement with the FESEM and AFM images in Fig. 3 and Figure S1, respectively. Indeed, in Fig. 6 the unetched HOPG samples have a consistently lower average growth at each number of the ALD cycles in the O1s/C1s(sp² and sp³), Al2p/C1s(sp² and sp³) and C1s(C-O)/C1s (sp² and sp³) ratios. However, these values are within the error bars of the HNO3-etched HOPG surface, suggesting that the -OH functional sites compare in reactivity to sp³ defect sites given that the same amount of Al₂O₃ is deposited. The difference in the growth of the Al₂O₃ on the oxidized HOPG compared to the unetched HOPG surface can be attributed to the increased density of functional sites from -OH and -COOH on the HOPG terrace region.

After 10 ALD cycles, it appears that there is a greater ALD growth rate from the Al2p/C1s(sp² and sp³) and O1s/C1s(sp² and sp³) ratios in Fig. 6. While linear ALD growth is expected after forming a film layer, initial submonolayer ALD growth is generally nonlinear [78]. This nonlinearity can be attributed to the reactivity of the oxygenated functional groups on the HOPG surface with the TMA precursor that is different from the film, thus affecting the initial growth rate. After the Al2O3 seed sites are created, post submonolayer growth, a different growth rate is expected for subsequent ALD deposition.

This XPS analysis on the terrace regions is compared with the morphological growth (see Figure S3 in supporting information), where subsequent Al_2O_3 growth is determined by the Al_2O_3 seeded sites on the surface from film growth after the initial reaction with TMA. What is interesting is that the surface topography before deposition appears to affect the subsequent Al_2O_3 deposition. A high density of functional sites, from both -OH and -COOH, are present on the HCl-etched HOPG terrace, so sites are available for reaction with the TMA precursor to produce the initial Al_2O_3 seeds for further nucleation. The XPS signals from the -COOH functional group is not plotted separately, as after the reaction with TMA, the -COOH sites would convert to a C-O species. The HNO3-etched HOPG surface is only functionalized with -OH groups, which are mainly focused at the step edges and patterned defect areas. The only functional sites on the untreated HOPG surface are sp³ sites at the square defect region and on step edges for facile reaction

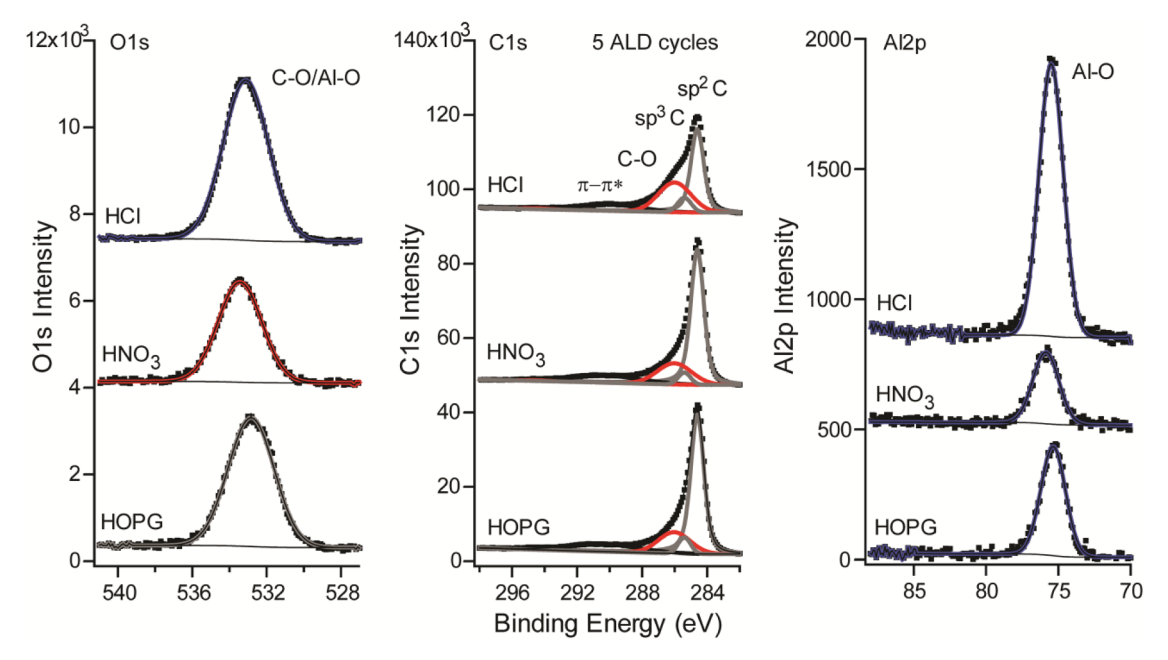


Fig. 5. Example XPS spectra of the O1s, C1s and Al2p regions after 5 ALD cycles show that Al₂O₃ was grown on HOPG and functionalized HOPG surfaces.

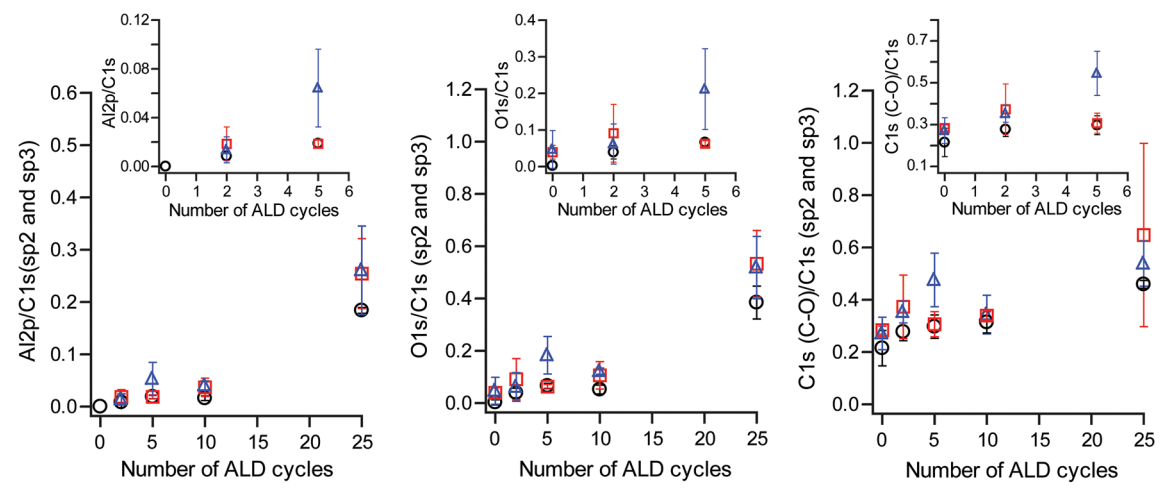


Fig. 6. Normalized XPS ratios, Al2p/C1s(sp² and sp³) ratio, O1s/C1s(sp² and sp³) ratio, C-O/C1s(sp² and sp³) ratio, of ALD Al₂O₃ cycles on HOPG (black circles), on HNO₃-etched HOPG (red squares) and HCl-etched HOPG (blue triangles).

with TMA and $\rm H_2O$. When $\rm Al_2O_3$ is deposited on the -OH or sp³ sites, there is a reaction and nucleation of $\rm Al_2O_3$, but at different sites compared to the HCl-etched HOPG. We infer that the reactivity of the surface is not only dependent on the type of functional group, but also on the density of functional groups (thus shown as different large scale morphologies) provided by the etching mechanism on the HOPG surface. This suggests that the order of reactivity of the TMA and $\rm H_2O$ on the oxidized and untreated HOPG surfaces is such (-COOH > -OH > sp³ > sp²).

Upon additional ALD cycles, beyond the submonolayer regime, growth occurs on the ${\rm Al_2O_3}$ seeded sites, assuming all the –OH or -COOH groups have reacted within the first two ALD cycles. At higher exposures, a film is grown on the HCl-etched HOPG sample suggesting Frank–van der Merwe growth, where the reaction occurs on the functional groups located on the terrace before filling in the square defect regions. The HCl-etched HOPG has a high density of –OH and –COOH functional groups that are more reactive compared to the sp³ sites in the patterned defect areas, thus providing the opportunity for film growth. This film growth is also observed on the untreated HOPG surfaces, but where the initial reaction and nucleation occurs at the sp³ defected (FIB

patterned) areas. Subsequent growth with additional ALD cycles then only occurs on the ${\rm Al_2O_3}$ areas resulting in Frank–van der Merwe growth selectively on the square defect areas. On the HNO₃-etched HOPG, particle nucleation occurs at select surface sites, presumably from the –OH functional sites, showing Volmer Weber-like growth at submonolayer ALD exposures [72]. At ALD exposures larger than 10 cycles, high-aspect ratio particles have nucleated and additional growth occurs on those sites, with the largest growth on the square defect areas. The untreated HOPG and HNO₃-treated HOPG surfaces seem to provide better surface sites for particle nucleation with high-aspect ratios, which is highly desirable for the catalyst growth, thus providing a method for selective deposition of high surface area particles for further reactions in catalytic mechanisms [1–4]. The HCl-etched HOPG shows promise for semiconductor applications where selective film growth at select areas could be controlled in the submonolayer coverage regime.

The samples were also analyzed after ALD using ATR-FTIR (not shown). However, due to the difficulty in movement and placement of the samples onto the ATR plate, in addition to small signals from submonolayer ALD, it was difficult to observe the Al-O stretch. A small shoulder was observed on samples that were exposed to at least 25 ALD

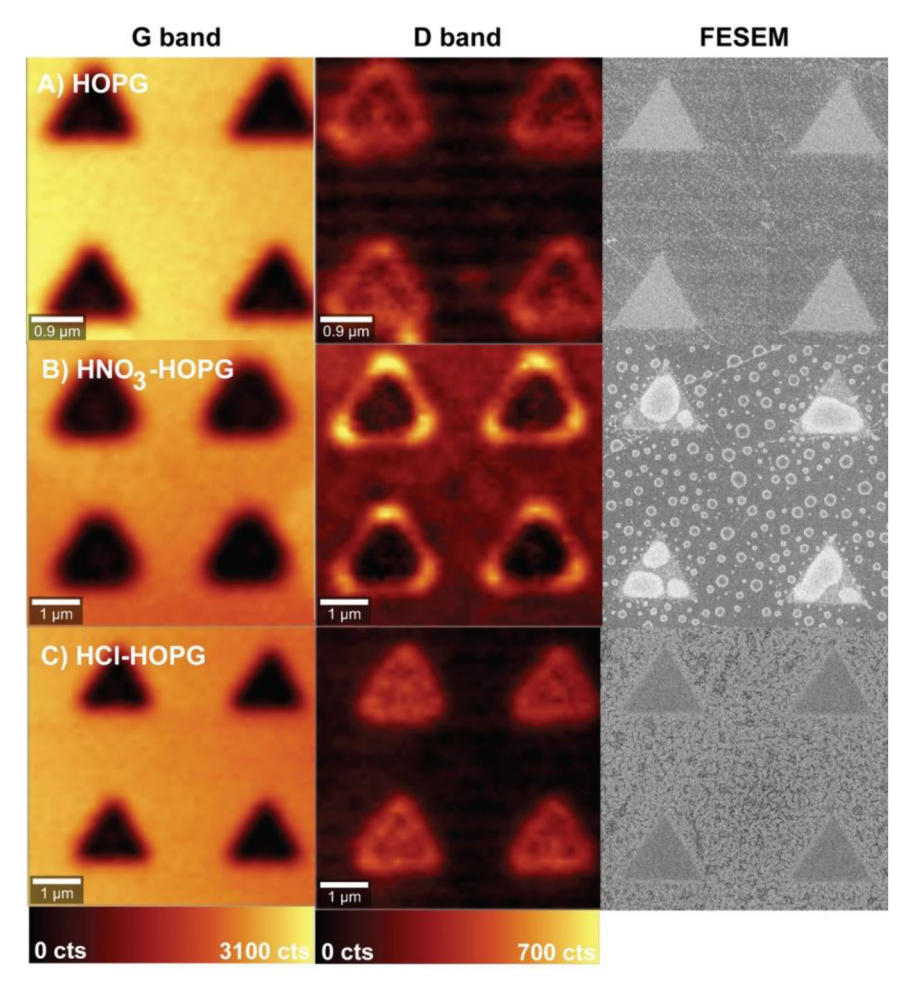


Fig. 7. Raman confocal images of Al_2O_3 (after 5 ALD cycles) on patterned triangular defects on HOPG: left column G-band signal images at 1575 cm⁻¹, middle column shows the p-band signal images at 1352 cm⁻¹, right column shows the corresponding FESEM images of the same samples.

cycles, near 970 cm $^{-1}$ for the Al-O stretch, indicating growth of ${\rm Al_2O_3}$ [75]. This spectral identification is better answered by the aforementioned XPS analysis discussed above.

Raman spectroscopy is an ideal technique to measure ordering of the surface of graphene and other carbon materials, where the G (E_{2g}) band is the in-plane C=C mode of the graphite sheets and the D-band is representative of the structural disorder in carbon materials (and inactive in infrared spectroscopy) [32,64,79–81]. Confocal Raman microscopy was used to map the G- and D-band intensities to measure how the defect regions (triangular shaped, in the presented data below) were affected by the acid etching and Al_2O_3 ALD growth.

Fig. 7 shows the Raman microscopy images of the G-band channels (1575 cm $^{-1}$) and the p-band channels (1352 cm $^{-1}$) [64,82] in comparison with the FESEM images for samples after 5 ALD cycles. These images are a three dimensional representation, where every pixel is a Raman spectrum and the intensity is scaled to the Raman intensity of the band (G or D) of interest. The top row shows the results for A) untreated HOPG, the second row shows results for B) HNO₃–etched HOPG and the bottom row shows results for C) HCl-etched HOPG. No Al₂O₃ signal was observed in the Raman spectrum in any of the ALD samples. The Raman spectra were acquired from samples exposed up to 50 ALD cycles (5.0 nm) on HOPG and still did not observe the predicted 750 cm $^{-1}$ Raman shift for Al₂O₃ [83,84]. Signficantly more ALD cycles may be required to produce enough material to observe the Raman spectral shifts of metal oxides grown by ALD.

In all images in Fig. 7 from the G-band channel, the signals appear the same, showing that the majority of the Raman signal detected on the terrace areas is from intact graphite layers. There is only signal from

the C=C bond from the terrace regions, outside the triangular defects. No functional groups were observed in the Raman spectra (shown in Figure S4, supporting information). In contrast, the images that show the D-band spectral images exhibit sharp differences from the growth of the Al₂O₃ on the triangular defect regions. On untreated HOPG (A), the D-band intensity arises from the triangular defect region with higher Dband signals on the edges of the triangles. This is a result from the Al₂O₃ growing as a film inside the entire triangular defect area, where the Dband signal is detected in the same area. This shows that although the Al₂O₃ growth was inside the triangular defect, the Al₂O₃ is semitransparent to the Raman imaging. On the HNO3-treated HOPG, 5 ALD cycles of Al₂O₃ grows as platelets, beginning at the defect edges, thus leaving a strong p-band intensity at the corners of the triangular defects. This suggests the platelets grow on the edges and on the bottom of the defect area, leaving the corners uncovered resulting in the strong Dband signal in Fig. 7. The lack of p-band signal inside the triangle signifies the presence of the Al₂O₃ particles at the patterned defects have blocked the remaining D-band signal. On the HCl-treated HOPG, the Dband signal is strongest inside the defect areas, as a result of the Al₂O₃ growth on the terrace sites, instead of in the defect areas, thus leaving the disordered graphite surface exposed in the patterned defects. These Raman images further clarify through spectral imaging where the Al₂O₃ nucleates and grows on the HOPG and functionalized HOPG.

Both the D and G bands are the most distinct features of graphitic materials that are well characterized using Raman spectroscopy. The D/G ratios of the Raman-shift intensities were analyzed to measure the effect of the oxidation and ALD [85,86]. For all samples, the I_D/I_G ratio remains approximately 0.1 for the untreated and HCl-etched HOPG and

0.2 for HNO $_3$ -etched HOPG measurements recorded on the terrace sites (outside the triangular defect area). Inside the defect areas on all surfaces, the I_D/I_G ratio was significantly higher at ~ 0.7 owing to the functional groups, grown Al_2O_3 and other structural disorder created from using the FIB to create the defect areas. We also measured the I_D/I_G ratio on the edges of the patterned defect area on HOPG and HNO $_3$ -etched HOPG. On those samples the ratio decreased to ~ 0.3 and 0.45, respectively, suggesting that the defect edges have less disorder than the defect area. One would expect the HCl-etched HOPG terraces to have a high I_D/I_G intensity ratio, due to the high density of functional groups. However, it is possible the Raman spectra imaging is not sensitive enough to detect these small changes (< 1 nm).

Overall, the effect of etching HOPG with strong acids produces functional (-OH and -COOH) groups that appear to produce different surface morphologies and therefore alter growth of Al₂O₃, as observed by XPS, AFM and FESEM. Different functional sites were produced at different locations and densities on the HOPG terrace and defect regions possibly due to the difference in etching mechanisms of HNO₃ and HCl, which we are currently investigating. Four different functional sites were produced and compared on the HOPG surface: -OH groups, -COOH groups, sp³ carbon sites, sp² carbon sites. The fact that a film was grown on the terrace region after etching with HCl compared to particle growth of high-aspect ratio on the defect sites of HOPG etched with HNO3 suggests that a high density of functional groups was produced on the HCl-treated surface compared to the HNO3-treated surface. Additionally, the reactivity of the functional groups on the surface with ALD cycles of TMA and H₂O also affect where the Al₂O₃ nucleates, in the order: $-COOH > -OH > sp^3 > sp^2$. This proposed reactivity is from the observation that there is more growth on the terraces of the HCl-etched HOPG compared to the growth in the defect regions on the untreated HOPG. Additionally, the HNO3-etched HOPG resulted in Al₂O₃ particle growth on the defect sites and pinholes on the terrace, presumably where the -OH functional groups reside. This can be compared to the untreated HOPG surfaces that only had sp² and sp³ carbon bonds. Here the Al₂O₃ was only found to grow on the sp³ defect regions, as it has been previously shown [28,40,87], from the reaction of TMA with the sp³ carbon (defects and edges).

The HCl etching of the terrace regions appears to result in a greater density of functional groups compared to HNO3-etched HOPG according to the FESEM images in Fig. 3. On the HCl-etched HOPG surface, the ${\rm Al}_2{\rm O}_3$ is grown on the -OH and -COOH functional groups on the terrace instead of the sp³ carbon bonds in the defected area, as was for the untreated HOPG, thus suggesting that the -COOH and -OH groups have a higher reactivity compared to the sp³ carbon bonds on the untreated HOPG surface. However it must be pointed out that this result could also simply be from the higher density of functional sites (overall more oxygenated sites). On the other hand, the XPS ratios in Fig. 6 suggest that there is more ${\rm Al}_2{\rm O}_3$ grown on the oxygenated HOPG supported by the microscopy images. Further *in situ* studies may be required to fully understand the impact of the OH and COOH functional sites on graphitic materials.

In summary, this study shows that TMA reacts selectively with oxygen functional sites in the classic ALD reaction to deposit and grow Al_2O_3 on functionalized HOPG. Activated area deposition is achieved by creating not only different functional sites, but also different densities of functional sites that create large scale topographical differences. These results suggest that deposition could be further controlled by understanding the etching mechanism of HCl, HNO_3 or other acids with graphene-based materials to connect the spectroscopic identification of the functional groups with the resulting surface topography.

At submonolayer coverage, Al_2O_3 deposits selectively on those functional sites. The placement of these functional sites is determined by the etching mechanism of the acid with the HOPG surface. These results suggest that the HCl-etched HOPG surface could yield a method for selective etching of certain regions of graphene, thus allowing for growth of insulating materials on specific regions. The creation of -OH

functional groups on defect sites by the HNO₃ could yield a method for growth of metal catalyst particles of high aspect ratio, desirable for controllable growth of heterogeneous catalysts.

4. Conclusions

We have shown that different etching of HOPG produces different morphologies and densities of functional sites that affect the nucleation and growth of ALD Al₂O₃ on HOPG. By understanding how HOPG is etched and functionalized by different acids, metal oxide deposition could be achieved by area activation for graphene-based materials. The surface was functionalized, using HCl and HNO₃, resulting in -OH and -COOH functional groups on the HOPG terrace using HCl and -OH functional groups on the defect sites using HNO3. The etching of the HOPG surface with two different acids affects the topography by producing different densities of functional sites and therefore the nucleation of Al₂O₃ using ALD. At submonolayer coverage, high surface area Al₂O₃ particles were grown on HNO₃-etched HOPG, whereas a film of Al2O3 was grown on the terrace regions of the HCl-treated HOPG surface. Depending on the application and whether a uniform film is required (semiconductor industry) versus particles that have high surface areas (catalysis industry) this method may provide unique opportunities for spatially controlled atomic layer growth of metal oxide structures without the use of protection layers.

Acknowledgements

This work was supported by startup funds from the Department of Chemistry, the College of Sciences and Arts, and the Office of Research REF-SEED at Michigan Technological University. The AFM was supported by the National Science Foundation MRI [grant: CHE 1725818]. A portion of this work was conducted in the Minnesota Nano Center, which is supported by the National Science Foundation through the National Nano Coordinated Infrastructure Network (NNCI) [Award Number ECCS-1542202]. The Raman microscopy was carried out in the Characterization Facility, University of Minnesota, which receives partial support from National Science Foundation through the MRSEC program (United States).

We acknowledge Tony Whipple, Gary Olin, and Paul Kimani for assistance with training and use of the ALD and ellipsometry measurements at the University of Minnesota Nano Center. We declare no competing research between University of Minnesota and Michigan Technological University. We also acknowledge the Applied Chemical & Morphological Analysis Laboratory (ACMAL) at Michigan Technological University for use of instruments and staff assistance, including Director Owen Mills, for training on the FESEM and FIB. We acknowledge Dr. Bahne C. Cornilsen for his intellectual contribution towards understanding Raman microscopy and Dr. Bing Luo for assistance with training on the confocal Raman microscope.

Author Contributions

M. Trought and K. Perrine prepared the samples at Michigan Tech and at the Univ. of Minnesota, performed the surface analysis, analyzed all data collected, and wrote the manuscript. T. Leftwich assisted with the XPS data collection and analysis, and reviewing & editing the manuscript. I. Wentworth and C. de Alwis assisted with sample preparation and FTIR analysis. K. Perrine conceptualized the project. All authors have given approval to the final version of the manuscript.

Supplementary materials

Supplementary material associated with this article can be found, in the online version, at doi:10.1016/j.susc.2019.121479.

References

- J.A. Singh, N.Y. Yang, S.F. Bent, Nanoengineering heterogeneous catalysts by atomic layer deposition, in: J.M. Prausnitz (Ed.) Annual Review of Chemical and Biomolecular Engineering, Vol 82017, pp. 41–62.
- [2] B.J. O'Neill, D.H.K. Jackson, J. Lee, C. Canlas, P.C. Stair, C.L. Marshall, J.W. Elam, T.F. Kuech, J.A. Dumesic, G.W. Huber, Catalyst design with atomic layer deposition, ACS Catal. 5 (2015) 1804–1825.
- [3] J.L. Lu, J.W. Elam, P.C. Stair, Atomic layer deposition-Sequential self-limiting surface reactions for advanced catalyst "bottom-up" synthesis, Surf. Sci. Rep. 71 (2016) 410–472.
- [4] A.J.M. Mackus, A.A. Bol, W.M.M. Kessels, The use of atomic layer deposition in advanced nanopatterning, Nanoscale 6 (2014) 10941–10960.
- [5] N.F.W. Thissen, R.H.J. Vervuurt, A.J.M. Mackus, J.J.L. Mulders, J.W. Weber, W.M.M. Kessels, A.A. Bol, Graphene devices with bottom-up contacts by area-selective atomic layer deposition, 2d Mater. 4 (2017).
- [6] N.P. Dasgupta, H.B.R. Lee, S.F. Bent, P.S. Weiss, Recent advances in atomic layer deposition, Chem. Mater. 28 (2016) 1943–1947.
- [7] J.W. Elam, N.P. Dasgupta, F.B. Prinz, ALD for clean energy conversion, utilization, and storage, Mrs. Bulletin 36 (2011) 899–906.
- [8] A.J.M. Mackus, N.F.W. Thissen, J.J.L. Mulders, P.H.F. Trompenaars, Z.H. Chen, W.M.M. Kessels, A.A. Bol, Resist-free fabricated carbon nanotube field-effect transistors with high-quality atomic-layer-deposited platinum contacts, Appl. Phys. Lett. 110 (2017).
- [9] A. Mameli, M.J.M. Merkx, B. Karasulu, F. Roozeboom, W.M.M. Kessels, A.J.M. Mackus, Area-Selective atomic layer deposition of SiO2 using acetylacetone as a chemoselective inhibitor in an ABC-Type cycle, ACS Nano 11 (2017) 0303-0311
- [10] A.J.M. Mackus, M.J.M. Merkx, W.M.M. Kessels, From the Bottom-Up: toward areaselective atomic layer deposition with high selectivity, Chem. Mater. 31 (2019) 2–12.
- [11] J.A. Singh, N.F.W. Thissen, W.H. Kim, H. Johnson, W.M.M. Kessels, A.A. Bol, S.F. Bent, A.J.M. Mackus, Area-Selective atomic layer deposition of metal oxides on noble metals through catalytic oxygen activation, Chem. Mater. 30 (2018) 663–670.
- [12] R.G. Closser, D.S. Bergsman, L. Ruelas, F.S.M. Hashemi, S.F. Bent, Correcting defects in area selective molecular layer deposition, J. Vac. Sci. Technol. A 35 (2017).
- [13] R.C. Longo, S. McDonnell, D. Dick, R.M. Wallace, Y.J. Chabal, J.H.G. Owen, J.B. Ballard, J.N. Randall, K. Cho, Selectivity of metal oxide atomic layer deposition on hydrogen terminated and oxidized Si(001)-(2×1) surface, J. Vac. Sci. Technol. B 32 (2014)
- [14] A.J.M. Mackus, S.A.F. Dielissen, J.J.L. Mulders, W.M.M. Kessels, Nanopatterning by direct-write atomic layer deposition, Nanoscale 4 (2012) 4477–4480.
- [15] S. George, Y. Lee, J. DuMont, N. Johnson, D. Zywotko, Atomic layer etching (ALE) using sequential thermal reactions: atomic layer deposition (ALD) in reverse, Abstr. Pap. Am. Chem. Soc. 253 (2017).
- [16] D.R. Zywotko, S.M. George, Thermal atomic layer etching of ZnO by a "Conversion-Etch" mechanism using sequential exposures of hydrogen fluoride and trimethylaluminum, Chem. Mater. 29 (2017) 1183–1191.
- [17] J. Lu, J.W. Elam, P.C. Stair, Synthesis and stabilization of supported metal catalysts by atomic layer deposition, Acc. Chem. Res. 46 (2013) 1806–1815.
- [18] R.L. Puurunen, Formation of metal oxide particles in atomic layer deposition during the chemisorption of metal chlorides: a review, Chem. Vap. Depos. 11 (2005) 79–90.
- [19] S.M. George, Atomic layer Deposition: an overview, Chem. Rev. 110 (2010) 111–131.
- [20] V. Miikkulainen, M. Leskela, M. Ritala, R.L. Puurunen, Crystallinity of inorganic films grown by atomic layer deposition: overview and general trends, J. Appl. Phys. 113 (2013).
- [21] S. Drewniak, R. Muzyka, A. Stolarczyk, T. Pustelny, M. Kotyczka-Moranska, M. Setkiewicz, Studies of reduced graphene oxide and graphite oxide in the aspect of their possible application in gas sensors, Sensors 16 (2016).
- [22] I. Wlasny, M. Rogala, P. Dabrowski, P.J. Kowalczyk, A. Busiakiewicz, W. Kozlowski, L. Lipinska, J. Jagiello, M. Aksienionek, Z. Sieradzki, I. Krucinska, M. Puchalski, E. Skrzetuska, Z. Draczynski, Z. Klusek, Finding optimal HBr reduction of inkjet printed graphene oxide for flexible electronics, Mater. Chem. Phys. 181 (2016) 409–414.
- [23] E.P. Randviir, D.A.C. Brownson, C.E. Banks, A decade of graphene research: production, applications and outlook, Mater. Today 17 (2014) 426–432.
- [24] Y.A. Chen, A. Star, S. Vidal, Sweet carbon nanostructures: carbohydrate conjugates with carbon nanotubes and graphene and their applications, Chem. Soc. Rev. 42 (2013) 4532–4542.
- [25] S. Wang, H. Sun, H.M. Ang, M.O. Tade, Adsorptive remediation of environmental pollutants using novel graphene-based nanomaterials, Chem. Eng. J. 226 (2013) 336–347.
- [26] M. Acik, Y.J. Chabal, Nature of graphene edges: a review, Jpn. J. Appl. Phys. 50 (2011).
- [27] B. Lee, G. Mordi, M.J. Kim, Y.J. Chabal, E.M. Vogel, R.M. Wallace, K.J. Cho, L. Colombo, J. Kim, Characteristics of high-k Al2O3 dielectric using ozone-based atomic layer deposition for dual-gated graphene devices, Appl. Phys. Lett. 97 (2010).
- [28] Y. Xuan, Y.Q. Wu, T. Shen, M. Qi, M.A. Capano, J.A. Cooper, P.D. Ye, Atomic-layer-deposited nanostructures for graphene-based nanoelectronics, Appl. Phys. Lett. 92 (2008).
- [29] V. Meunier, A.G. Souza, E.B. Barros, M.S. Dresselhaus, Physical properties of low-

- dimensional sp(2)-based carbon nanostructures, Rev. Mod. Phys. 88 (2016).
- [30] D.R. Dreyer, S. Park, C.W. Bielawski, R.S. Ruoff, The chemistry of graphene oxide, Chem. Soc. Rev. 39 (2010) 228–240.
- [31] S.V. Morozov, K.S. Novoselov, M.I. Katsnelson, F. Schedin, D.C. Elias, J.A. Jaszczak, A.K. Geim, Giant intrinsic carrier mobilities in graphene and its bilayer, Phys. Rev. Lett. 100 (2008).
- [32] M.S. Dresselhaus, Fifty years in studying carbon-based materials, Phys. Scr. T146 (2012).
- [33] M. Rogala, P.J. Kowalczyk, P. Dabrowski, I. Wlasny, W. Kozlowski, A. Busiakiewicz, S. Pawlowski, G. Dobinski, M. Smolny, I. Karaduman, L. Lipinska, R. Kozinski, K. Librant, J. Jagiello, K. Grodecki, J.M. Baranowski, K. Szot, Z. Klusek, The role of water in resistive switching in graphene oxide, Appl. Phys. Lett. 106 (2015).
- [34] X.R. Wang, S.M. Tabakman, H.J. Dai, Atomic layer deposition of metal oxides on pristine and functionalized graphene, J. Am. Chem. Soc. 130 (2008) 8152 -+.
- [35] J. Yang, J.L. Bitter, B.A. Smith, D.H. Fairbrother, W.P. Ball, Transport of oxidized multi-walled carbon nanotubes through silica based porous Media: influences of aquatic Chemistry, surface Chemistry, and natural organic matter, Environ. Sci. Technol. 47 (2013) 14034–14043.
- [36] R.C. Longo, J.H.G. Owen, S. McDonnell, D. Dick, J.B. Ballard, J.N. Randall, R.M. Wallace, Y.J. Chabal, K. Cho, Toward atomic-scale patterned atomic layer Deposition: reactions of Al2O3 precursors on a Si(001) surface with mixed functionalizations, J. Phys. Chem. C 120 (2016) 2628–2641.
- [37] K.A. Wepasnick, B.A. Smith, K.E. Schrote, H.K. Wilson, S.R. Diegelmann, D.H. Fairbrother, Surface and structural characterization of multi-walled carbon nanotubes following different oxidative treatments, Carbon 49 (2011) 24–36.
- [38] M. Rogala, P. Dabrowski, P.J. Kowalczyk, I. Wlasny, W. Kozlowski, A. Busiakiewicz, I. Karaduman, L. Lipinska, J.M. Baranowski, Z. Klusek, The observer effect in graphene oxide - How the standard measurements affect the chemical and electronic structure, Carbon 103 (2016) 235–241.
- [39] A.M. Dimiev, J.M. Tour, Mechanism of graphene oxide formation, ACS Nano 8 (2014) 3060–3068.
- [40] B.K. Lee, S.Y. Park, H.C. Kim, K. Cho, E.M. Vogel, M.J. Kim, R.M. Wallace, J.Y. Kim, Conformal Al2O3 dielectric layer deposited by atomic layer deposition for graphene-based nanoelectronics, Appl. Phys. Lett. 92 (2008).
- [41] H.B.R. Lee, S.F. Bent, Formation of continuous pt films on the graphite surface by atomic layer deposition with reactive O-3, Chem. Mater. 27 (2015) 6802–6809.
- [42] J.S. King, A. Wittstock, J. Biener, S.O. Kucheyev, Y.M. Wang, T.F. Baumann, S.K. Giri, A.V. Hamza, M. Baeumer, S.F. Bent, Ultralow loading pt nanocatalysts prepared by atomic layer deposition on carbon aerogels, Nano Lett. 8 (2008) 2405–2409.
- [43] K. Kim, H.B.R. Lee, R.W. Johnson, J.T. Tanskanen, N. Liu, M.G. Kim, C. Pang, C. Ahn, S.F. Bent, Z.N. Bao, Selective metal deposition at graphene line defects by atomic layer deposition, Nat. Commun. 5 (2014).
- [44] Y.J. Zhu, A. Schnieders, J.D. Alexander, T.P. Beebe, Pit-templated synthesis and oxygen adsorption properties of gold nanostructures on highly oriented pyrolytic graphite, Langmuir 18 (2002) 5728–5733.
- [45] C.E. Cross, J.C. Hemminger, R.M. Penner, Physical vapor deposition of one-dimensional nanoparticle arrays on graphite: seeding the electrodeposition of gold nanowires, Langmuir 23 (2007) 10372–10379.
- [46] B.J. Murray, Q. Li, J.T. Newberg, J.C. Hemminger, R.M. Penner, Silver oxide microwires: electrodeposition and observation of reversible resistance modulation upon exposure to ammonia vapor, Chem. Mater. 17 (2005) 6611–6618.
- [47] J. Taing, M.H. Cheng, J.C. Hemminger, Photodeposition of ag or pt onto TiO2 nanoparticles decorated on step edges of HOPG, ACS Nano 5 (2011) 6325–6333.
- [48] R. Bavand, A. Yelon, E. Sacher, X-ray photoelectron spectroscopic and morphologic studies of ru nanoparticles deposited onto highly oriented pyrolytic graphite, Appl. Surf. Sci. 355 (2015) 279–289.
- [49] D. Appy, H.P. Lei, C.Z. Wang, M.C. Tringides, D.J. Liu, J.W. Evans, P.A. Thiel, Transition metals on the (0001) surface of graphite: fundamental aspects of adsorption, diffusion, and morphology, Prog. Surf. Sci. 89 (2014) 219–238.
- [50] W. Luo, W. van der Veer, P. Chu, D.L. Mills, R.M. Penner, J.C. Hemminger, Polarization-dependent surface enhanced Raman scattering from silver 1D nanoparticle arrays, J. Phys. Chem. C 112 (2008) 11609–11613.
- [51] E.C. Walter, M.P. Zach, F. Favier, B.J. Murray, K. Inazu, J.C. Hemminger, R.M. Penner, Metal nanowire arrays by electrodeposition, ChemPhysChem 4 (2003) 131–138.
- [52] Y.H. Zhou, A. Lii-Rosales, M. Kim, M. Wallingford, D.P. Jing, M.C. Tringides, C.Z. Wang, P.A. Thiel, Defect-mediated, thermally-activated encapsulation of metals at the surface of graphite, Carbon 127 (2018) 305–311.
- [53] K.S. Novoselov, A.K. Geim, S.V. Morozov, D. Jiang, Y. Zhang, S.V. Dubonos, I.V. Grigorieva, A.A. Firsov, Electric field effect in atomically thin carbon films, Science 306 (2004) 666–669.
- [54] Y.R. Shin, S.M. Jung, I.Y. Jeon, J.B. Baek, The oxidation mechanism of highly ordered pyrolytic graphite in a nitric acid/sulfuric acid mixture, Carbon 52 (2013) 493–498.
- [55] R. Burgess, C. Buono, P.R. Davies, R.J. Davies, T. Legge, A. Lai, R. Lewis, D.J. Morgan, N. Robinson, D.J. Willock, The functionalisation of graphite surfaces with nitric acid: identification of functional groups and their effects on gold deposition, J. Catal. 323 (2015) 10–18.
- [56] A. Rodriguez-Fortea, M. Iannuzzi, M. Parrinello, Ab initio molecular dynamics study of heterogeneous oxidation of graphite by means of gas-phase nitric acid, J. Phys. Chem. B 110 (2006) 3477–3484.
- [57] E.J. Moler, S.A. Kellar, Z. Hussain, Y.F. Chen, D.A. Shirley, W.R.A. Huff, Z.Q. Huang, Direct evidence for the nature of core-level photoemission satellites using angle-resolved photoemission extended fine structure, Phys. Rev. B 56 (1997) 16016–16020.

[58] J.A. Leiro, M.H. Heinonen, T. Laiho, I.G. Batirev, Core-level XPS spectra of fullerene, highly oriented pyrolitic graphite, and glassy carbon, J. Electron Spectros. Relat. Phenomena 128 (2003) 205–213.

- [59] M.P. Seah, I.S. Gilmore, S.J. Spencer, I. Quantitative XPS, Analysis of X-ray photoelectron intensities from elemental data in a digital photoelectron database, J. Electron Spectros. Relat. Phenomena 120 (2001) 93–111.
- [60] S. Tougaard, C. Jansson, Comparison of validity and consistency of methods for quantitative XPS peak analysis, Surf. Interface Anal. 20 (1993) 1013–1046.
- [61] S. Hufner, G.K. Wertheim, J.H. Wernick, XPS core line asymmetries in metals, Solid State Commun. 17 (1975) 417–422.
- [62] S. Doniach, M. Sunjic, Many-electron singularity in X-ray photoemission and X-ray line spectra from metals, J. Phys. Part C Solid State Phys. 3 (1970) 285 -&.
- [63] B. Bowden, M. Davies, P.R. Davies, S. Guan, D.J. Morgan, V. Roberts, D. Wotton, The deposition of metal nanoparticles on carbon surfaces: the role of specific functional groups, Faraday Discuss. 208 (2018) 455–470.
- [64] Y. Wang, D.C. Alsmeyer, R.L. McCreery, Raman-spectroscopy of carbon materials structural basis of observed spectra, Chem. Mater. 2 (1990) 557–563.
- [65] R.J. Hamers, C. Stavis, A. Pokhrel, R. Franking, R.E. Ruther, X.Y. Wang, M.C. Cooperrider, H.J. Zheng, J.A. Carlisle, J.E. Butler, Characterization of molecular and biomolecular layers on diamond thin films by infrared reflection-absorption spectroscopy, Diam. Relat. Mater. 20 (2011) 733–742.
- [66] C. Buono, P.R. Davies, R.J. Davies, T. Jones, J. Kulhavy, R. Lewis, D.J. Morgan, N. Robinson, D.J. Willock, Spectroscopic and atomic force studies of the functionalisation of carbon surfaces: new insights into the role of the surface topography and specific chemical states, Faraday Discuss. 173 (2014) 257–272.
- [67] S. Paulose, R. Raghavan, B.K. George, Graphite oxide-iron oxide nanocomposites as a new class of catalyst for the thermal decomposition of ammonium perchlorate, RSC Adv. 6 (2016) 45977–45985.
- [68] M.J. Young, C.B. Musgrave, S.M. George, Growth and characterization of Al2O3 atomic layer deposition films on sp(2)-Graphitic carbon substrates using NO2/Trimethylaluminum pretreatment, ACS Appl. Mater. Interfaces 7 (2015) 12030–12037.
- [69] J. Avila, I. Razado, S. Lorcy, R. Fleurier, E. Pichonat, D. Vignaud, X. Wallart, M.C. Asensio, Exploring electronic structure of one-atom thick polycrystalline graphene films: a nano angle resolved photoemission study, Sci. Rep. 3 (2013).
- [70] H. Estrade-Szwarckopf, XPS photoemission in carbonaceous materials: a "defect" peak beside the graphitic asymmetric peak, Carbon 42 (2004) 1713–1721.
- [71] D.Q. Yang, E. Sacher, Carbon 1 s X-ray photoemission line shape analysis of highly oriented pyrolytic graphite: the influence of structural damage on peak asymmetry, Langmuir 22 (2006) 860–862.
- [72] B.F. Usher. The contribution of kinetic nucleation theories to studies of volmer-

- weber thin-film growth, Appl. Surf. Sci. 22-3 (1985) 506-511.
- [73] L. Zheng, X.H. Cheng, D. Cao, G. Wang, Z.J. Wang, D.W. Xu, C. Xia, L.Y. Shen, Y.H. Yu, D.S. Shen, Improvement of Al2O3 films on graphene grown by atomic layer deposition with Pre-H2O treatment, ACS Appl. Mater. Interfaces 6 (2014) 7014–7019.
- [74] S. McDonnell, A. Pirkle, J. Kim, L. Colombo, R.M. Wallace, Trimethyl-aluminum and ozone interactions with graphite in atomic layer deposition of Al2O3, J. Appl. Phys. 112 (2012).
- [75] D.N. Goldstein, J.A. McCormick, S.M. George, Al(2)O(3) atomic layer deposition with trimethylaluminum and ozone studied by in situ transmission FTIR spectroscopy and quadrupole mass spectrometry, J. Phys. Chem. C 112 (2008) 19530–19539.
- [76] C. Marichy, N. Pinna, Carbon-nanostructures coated/decorated by atomic layer deposition: growth and applications, Coord. Chem. Rev. 257 (2013) 3232–3253.
- [77] H.G. Kim, H.B.R. Leek, Atomic layer deposition on 2D materials, Chem. Mater. 29 (2017) 3809–3826.
- [78] J. Kim, T.W. Kim, Initial surface reactions of atomic layer deposition, JOM 61 (2009) 17–22.
- [79] R. Saito, M. Hofmann, G. Dresselhaus, A. Jorio, M.S. Dresselhaus, Raman spectroscopy of graphene and carbon nanotubes, Adv. Phys. 60 (2011) 413–550.
- [80] A. Merlen, J.G. Buijnsters, C. Pardanaud, A guide to and review of the use of multiwavelength raman spectroscopy for characterizing defective aromatic carbon solids: from graphene to amorphous carbons, Coatings 7 (2017).
- [81] R. Beams, L.G. Cancado, L. Novotny, Raman characterization of defects and dopants in graphene, J. Phys.-Condens. Matter 27 (2015).
- [82] Y. Kawashima, G. Katagiri, Fundamentals, overtones, and combinations in the Raman-spectrum of graphite, Phys. Rev. B 52 (1995) 10053–10059.
- [83] Y. Gao, H. Leiste, S. Heissler, S. Ulrich, M. Stueber, Optical properties of radio-frequency magnetron sputtered alpha-(Cr1-xAlx)(2)O-3 thin films grown on alpha-Al2O3 substrates at different temperatures, Thin Solid Films 660 (2018) 439–446.
- [84] B. Lafuente, R.T. Downs, H. Yang, N. Stone, The power of databases: the RRUFF project, in: T. Armbruster, R.M. Danisi (Eds.), Highlights in Mineralogical Crystallography, Berlin, Germany, W. De Gruyter, 2015, pp. 1–30.
- [85] P. Lespade, A. Marchand, M. Couzi, F. Cruege, Characterization of carbon materials with Raman microspectrometry. Carbon 22 (1984) 375–385.
- [86] D.S. Knight, Characterization of diamonds, synthetic diamond films and related carbon materials by Raman-spectroscopy, Abstr. Pap. Am. Chem. Soc. 202 (1991) 118-PHYS.
- [87] G.B. Barin, A.G. Souza, L.S. Barreto, J. Kong, Pre-Patterned CVD Graphene: insights on ALD deposition parameters and their influence on Al2O3 and graphene layers, Mrs Adv. 1 (2016) 1401–1409.